

First-principles study on the mobility of screw dislocations in bcc iron

M. Itakura^{a,*}, H. Kaburaki^b, M. Yamaguchi^b

^a Center for Computational Science & e-Systems, Japan Atomic Energy Agency, 5-1-5 Kashiwanoha, Kashiwa, Chiba 277-8587, Japan

^b Center for Computational Science & e-Systems, Japan Atomic Energy Agency, 2-4 Shirakata-Shirane, Tokai-mura, Naka-gun, Ibaraki 319-1184, Japan

Received 10 November 2011; received in revised form 19 March 2012; accepted 19 March 2012

Available online 30 April 2012

Abstract

The fully two-dimensional Peierls barrier map of screw dislocations in body-centered cubic (bcc) iron has been calculated using the first-principles method to identify the migration path of a dislocation core. An efficient method to correct the effect of the finite size cell used in the first-principles method on the energy of a lattice defect was devised to determine the accurate barrier profile. We find that the migration path is close to a straight line that is confined in a {110} plane and the Peierls barrier profile is single humped. This result clarifies why the existing empirical potentials of bcc iron fail to predict the correct mobility path. A line tension model incorporating these first-principles calculation results is used to predict the kink activation energy to be 0.73 eV in agreement with experiment.

© 2012 Acta Materialia Inc. Published by Elsevier Ltd. All rights reserved.

Keywords: First-principles calculation; Dislocations; Peierls barrier; Plastic deformation

1. Introduction

Recent nanopillar and nanowire experiments [1], as well as in situ observation of dislocation motions [2], clearly demonstrate the highly peculiar natures of plasticity in body-centered cubic (bcc) metals. Plasticity in bcc metals is mainly mediated by the thermal activation of kink pairs in screw dislocation lines owing to strong lattice friction, and shows a strong dependence on the metal elements, the direction of the applied stress and temperature [3,4]. In face-centered cubic metals, the lattice friction is extremely weak and a dislocation motion can be described well by the universal model of phonon drag. Therefore, a reliable model of dislocation mobility in bcc metals is indispensable for simulating plastic deformation in such metals.

One of the remarkable properties of a screw dislocation in bcc metals is that its motion is not confined in a plane but varies with the orientation of the applied stress. An improper model leads not only to qualitatively incorrect mobility but also to a quantitatively wrong direction of migration. Fig. 1 shows several possible migration paths

for a screw dislocation which moves from one stable “easy-core” position to another. There are several unstable or metastable dislocation positions, which are referred to as “hard-core” and “split-core” positions. Middle points between easy-core positions (M points) are also shown in Fig. 1.

Anisotropic linear elasticity solutions (LES) for each dislocation configuration seen from the [111] direction are shown in Fig. 2 using the differential displacement map (see Appendix A). The positive and negative numbers in the figure represent the helicity of the dislocation core. The solution for the M point is obtained by a simple interpolation between the solutions of two adjacent easy-core configurations. This solution can be regarded as the sum of displacement fields induced by two “half” dislocation helicities located at the two easy-core positions. The solution for the split-core configuration can then be obtained by linear extrapolation using the hard-core configuration and the M point configuration. This solution can be regarded as the sum of displacement fields induced by two positive dislocations at the easy-core positions and one negative dislocation at the hard-core position. Note that the LES for the easy-core and hard-core configurations have D_3 point group symmetry in Fig. 2, as is also

* Corresponding author.

E-mail address: itakura.mitsuhiro@jaea.go.jp (M. Itakura).

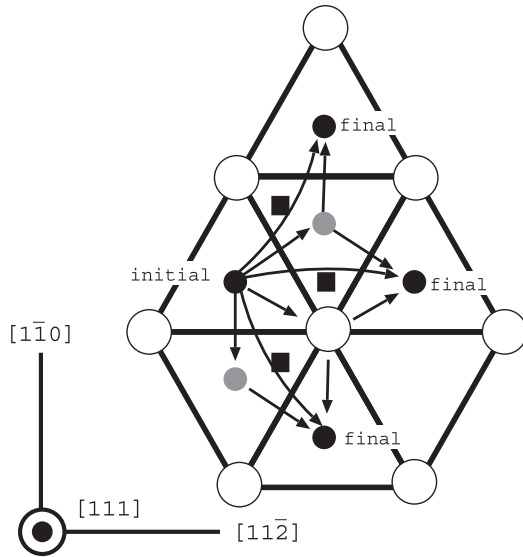


Fig. 1. Several possible migration paths of a screw dislocation in bcc metals. Black, gray and white circles represent the dislocation center positions of easy-core, hard-core and split-core configurations, respectively. Black squares are the middle points between easy-core positions (M points). Metal atoms are located at the white circles.

true for the results of density functional theory (DFT) calculations for bcc iron and other bcc metals [5–8]. We will later see that the displacement of the elasticity solutions for the split-core and M point configurations is also close to that of the DFT calculations.

If either the hard-core or split-core configuration is metastable, the migration of a dislocation follows a bent line and the Peierls energy becomes double humped. On the other hand, when neither of the intermediate configurations is metastable, the path is close to a straight line

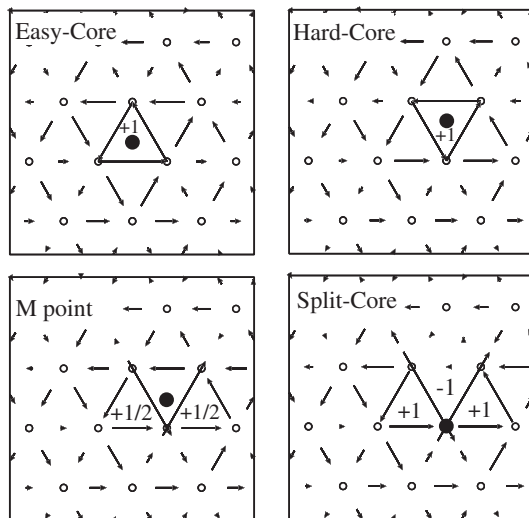


Fig. 2. Differential displacement maps of the linear elasticity solution for easy-core, hard-core, M point and split-core configurations. Filled circles indicate the dislocation core position in each configuration; the positive and negative numbers indicate the dislocation helicity located at each triangle. See the main text for details.

and the Peierls energy becomes single humped. The difference in this energy landscape strongly affects the kink nucleation energy of a screw dislocation in different slip directions, and this determines not only the average migration velocity but also the average migration direction. Indeed, strong temperature and stress dependence on the average migration direction of a screw dislocation is reported in a molecular dynamics study of bcc iron screw dislocation [9].

However, since no quantum mechanical data of dislocation movement are used for the fitting of the empirical potential of bcc iron employed in Ref. [9], the dislocation motion obtained in the molecular dynamics (MD) simulations should critically be checked by the DFT-based simulations. The Peierls energy in bcc iron without shear stress has been calculated by Ventelon and Willaime [10] using the DFT method with a localized basis. In the present work we employ the more accurate plane-wave-based DFT to calculate a Peierls energy of an isolated screw dislocation core with and without the applied shear stress, obtain a complete Peierls barrier map for the two-dimensional motion of a screw dislocation and identify its migration path. By coupling the DFT result with the line tension model of a dislocation, we also estimate the average slip direction of screw dislocations for various temperatures and applied stresses.

This paper is organized as follows. We first describe the method used for the DFT calculations. Further details of the DFT calculations to estimate the Peierls energy are dealt with in Section 3. In Section 4 we describe a method to estimate and correct the finite size effect of the DFT calculations using the Green's function method. In Section 5 the results of the DFT calculations are summarized. Section 6 presents the line tension model of a dislocation to estimate the kink pair nucleation energy for various applied stresses. Concluding remarks are given in Section 7.

2. The method of DFT calculations

The electronic structure calculations and the structure relaxations by force minimizations in the DFT steps are performed using the Vienna ab initio simulation package, with the projector augmented wave method and ultrasoft pseudopotentials. The exchange correlation energy is calculated by the generalized gradient approximation. Spin-polarized calculations are employed in all cases. The Methfessel–Paxton smearing method with 0.1-eV width is used. Structural relaxation is terminated when the maximum force acting on the movable degrees of freedom becomes less than $10 \text{ meV } \text{\AA}^{-1}$. The error of energy that comes from this termination is estimated to be 2 meV by comparing the energy with the calculation for the smaller threshold of $3 \text{ meV } \text{\AA}^{-1}$. The cutoff energy for the plane wave basis set is 400 eV, and the convergence of Peierls barrier energy with respect to the increasing cutoff is confirmed. The cutoff energy for the augmentation charges is 511.368 eV.

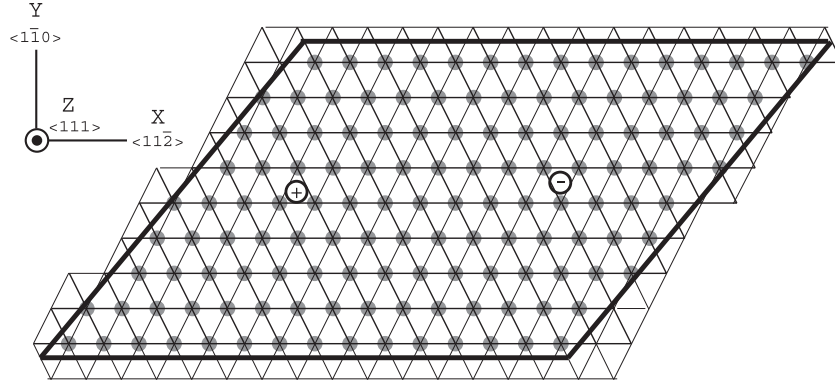


Fig. 3. Periodic quadrupolar array of dislocation cores in a parallelepiped cell used in the DFT calculations, seen from the $[1\ 1\ 1]$ direction. Gray circles are iron atoms and the two white circles are the two dislocations with opposite helicities.

Periodic dislocation quadrupole configurations in a parallelepiped cell shown in Fig. 3 defined by the following three edges,

$$\begin{aligned} \mathbf{e}_1 &= L_x \mathbf{v}_{112}, \\ \mathbf{e}_2 &= \frac{L_x}{2} \mathbf{v}_{112} + L_y \mathbf{v}_{110} + \frac{1}{2} \mathbf{v}_{111} \\ \mathbf{e}_3 &= \mathbf{v}_{111} \end{aligned} \quad (1)$$

are used in all calculations, where $\mathbf{v}_{112} = a_0[1\ 1\ 2]/3$, $\mathbf{v}_{110} = a_0[1\ 1\ 0]$, $\mathbf{v}_{111} = a_0[1\ 1\ 1]/2$ and $a_0 = 2.833\ \text{\AA}$ is a lattice parameter estimated by a calculation of single bcc cell of $[a_0 0 0] \times [0 a_0 0] \times [0 0 a_0]$ with $20 \times 20 \times 20$ k -points. DFT calculations are mainly carried out on the $L_x \times L_y = 15 \times 9$ lattice, and the smaller and larger lattice sizes of $L_x \times L_y = 9 \times 5$, 9×7 , 15×7 , 21×11 are also employed to estimate the finite size effect. Hereafter we introduce the Cartesian coordinates X , Y and Z , which are parallel to the $[1\ 1\ 2]$, $[1\ 1\ 0]$ and $[1\ 1\ 1]$ directions, respectively. Two dislocations with opposite helicity are placed in the cell to form a periodic quadrupolar array.

The reciprocal lattice vectors of the parallelepiped described above are $(k_x, -k_y/2, 0)$, $(0, k_y, 0)$ and $(0, -k_y/2, k_z)$, where $k_x = \sqrt{6}\pi/(2a_0L_x)$, $k_y = \sqrt{2}\pi/(2a_0L_y)$ and $k_z = 2\sqrt{3}\pi/(3a_0)$. Since the Monkhorst–Pack k -point mesh for this inclined Brillouin zone breaks the symmetry of the independent inversions in the X , Y and Z directions, we use a Cartesian k -mesh of size $k_x/n_x \times k_y/2n_y \times k_z/16$, which preserves the symmetry. The mesh numbers n_x and n_y are adjusted so that the mesh size becomes close to $0.1\ \text{\AA}^{-1}$. Convergence of the Peierls barrier energy with respect to the increasing mesh number is confirmed.

3. Calculation of the Peierls barrier

We denote the displacement of each atom relative to the perfect crystal position by $\vec{u}_i = (u_i^x, u_i^y, u_i^z)$, where i is an index of an atom. We also define a differentiated displacement as the normalized difference of the Z -component displacement for each pair of neighbor atoms $u_{ij} = (u_i^z - u_j^z)/b$, where b denotes the length of the Burgers vector. For both \vec{u} and u_{ij} ,

the minimum image convention in the z axis is applied, and $|u_{ij}| \leq 1/2$ is always satisfied. We define the two-dimensional Peierls energy as the minimum energy under the constraint of dislocation location being at a certain position in the two-dimensional plane. By watching the differentiated displacement u_{ij} , one can determine in which triangle a dislocation is located: a directed sum of three u_{ij} around a triangle is equal to the dislocation helicity inside it.

It is easy to show that a set of possible values of three u_{ij} s around a triangle which has non-zero dislocation helicity becomes an equilateral triangle in the three-dimensional space of u_{ij} . Thus it would be natural to map this triangular region of u_{ij} to the triangle in the real space which surrounds the dislocation to define the intra-triangular dislocation position. Its explicit definition is given as:

$$\vec{P} = -2(\vec{r}_1 u_{32} + \vec{r}_2 u_{13} + \vec{r}_3 u_{21}) \quad (2)$$

where \vec{r}_i is the two-dimensional position of vertex i relative to the center of the triangle, as shown in Fig. 4. The position is relative to the center of the triangle. The Cartesian coordinate of the position is given as:

$$P_x = \frac{2\sqrt{2}}{3}(2u_1^z - u_2^z - u_3^z), \quad P_y = \frac{2\sqrt{6}}{3}(u_2^z - u_3^z)$$

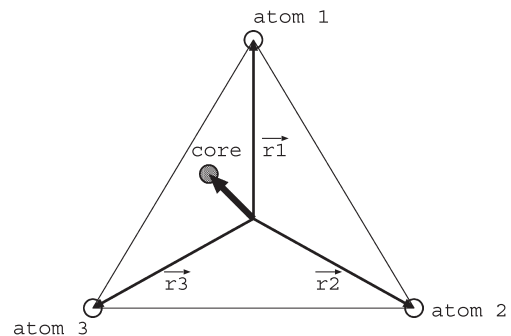


Fig. 4. Dislocation core position given by $-2(\vec{r}_1 u_{32} + \vec{r}_2 u_{13} + \vec{r}_3 u_{21})$, where \vec{r}_i is the position of vertex i relative to the center of the triangle. See the main text for details.

For a given dislocation position (P_x, P_y) , we define the Peierls energy $E_P(P_x, P_y)$ as follows:

$$E_P(P_x, P_y) = E_d(x^d) = \min_{x^o} E(x^d, x^o) = E(x^d, \bar{x}^o(x^d)) \quad (3)$$

where x^d denotes a set of degrees of freedom that is related to the dislocation position and is determined by (P_x, P_y) . The set of all the other degrees of freedom is denoted by x^o . In the present case, x^d are the Z displacements of the three atoms around a dislocation. The energy $E_d(x^d)$ is a minimum of the total energy $E(x^d, x^o)$ for a given value of x^d , and $\bar{x}^o(x^d)$ gives the values of x^o which minimizes the energy.

In the DFT calculations or MD simulations, $E_d(x^d)$ can be easily obtained by fixing the values of x^d and relaxing all the other degrees of freedom. Moreover, one can calculate the derivative of $E_d(x^d)$ with respect to one of the fixed degrees of freedom x_i^d from the forces acting on x_i^d , which are also easily obtained, as follows:

$$\begin{aligned} \frac{\partial E_d(x^d)}{\partial x_i^d} &= \frac{\partial E(x^d, \bar{x}^o(x^d))}{\partial x_i^d} \\ &= \frac{\partial E(x^d, x^o)}{\partial x_i^d} + \frac{\partial E(x^d, x^o)}{\partial x^o} \frac{\partial \bar{x}^o(x^d)}{\partial x_i^d} = -F_i \end{aligned} \quad (4)$$

where F_i is just a force acting on x_i^d . The term $\partial E(x^d, x^o)/\partial x^o$ is zero at \bar{x}^o because it gives minimum of $E(x^d, x^o)$ with respect to x^o . The force acting on the dislocation is calculated as follows:

$$\begin{aligned} -\frac{\partial E_P}{\partial P_x} &= \frac{\sqrt{2}}{8} (2F_1^z - F_2^z - F_3^z), \\ -\frac{\partial E_P}{\partial P_y} &= \frac{\sqrt{6}}{8} (F_2^z - F_3^z) \end{aligned} \quad (5)$$

It should be noted that the core position does not change when the three atoms move in the Z direction by the same amount d , and from the translational symmetry, E_d also remains unchanged. When there are two or more dislocations in the system separated by a long enough distance, the energy difference induced by independent translations of x_d for each dislocation mainly comes from the long-range elastic interaction between two dislocations, and is minimized by using the values of x_d given by a linear elasticity solution.

In general, the Peierls energy E_P as a function of the dislocation position P is discontinuous at the boundary between two triangles, since the choice of x_d differs in each triangle and different values of \bar{x}^o are obtained for different minimization conditions. To deal with this discontinuity, we extend the mapping domain of Eq. (2) in a hard-core triangle to include three adjacent easy-core positions, as shown in Fig. 5. The values of u_{ij} which correspond to these three extended vertexes becomes $u_{ij} = \pm 1/3$ on the boundary edge between the current hard-core and adjacent easy-core triangle and $u_{ij} = \mp 1/6$ on the two other edges. (Note that when the dislocation position crosses over a boundary between two triangles, u_{ij} on the boundary edge

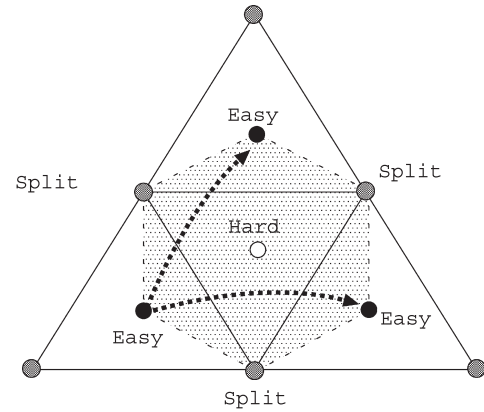


Fig. 5. The domain of mapping between the core position and the Z -displacement of three atoms around a hard-core position is extended to a regular hexagon which includes three adjacent easy-core positions.

discontinuously changes from $1/2$ to $-1/2$ if the minimum image convention is used. Instead, we allow u_{ij} to become larger than $1/2$ outside the original triangle so that the position given by Eq. (2) becomes continuous.) These coincide with the values of u_{ij} when the dislocation is at the center of the adjacent easy-core triangle if the easy-core state is D_3 symmetric, as is the case of bcc iron.

Therefore, by controlling the Z displacement of the three atoms around a hard-core triangle and relaxing all the other degrees of freedom, we can obtain a hard-core configuration, three adjacent easy-core configurations and any intermediate configurations between them. A continuous energy landscape of an area which covers all the relevant configurations for a dislocation core migration is also obtained. Later we will see that the split-core configuration has a very high energy according to the first-principles calculation, in contrast to the MD empirical potential calculation, and the migration path does not approach the split-core vertexes in the hexagon but always remains inside the hexagon.

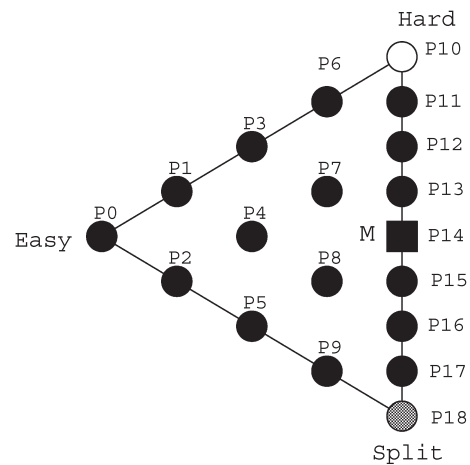


Fig. 6. The intra-triangular positions P0–P18 used in the DFT calculations.

From the symmetry, the energy landscape inside a hexagon can be determined by investigating the energy inside a triangle the three vertexes of which are easy-core, hard-core and split-core positions. Peierls energies for the intra-triangular positions denoted by P0–P18 shown in Fig. 6 are calculated using the DFT, and the two dislocations are set to the same intra-triangular position.

4. Finite size effects

Clouet et al. [11] showed that the difference in the dislocation displacement fields between LES and the DFT calculation can be described well by the line forces near the core, which come from the heavily displaced atoms at the core region. While this “core force” is very localized at the core region, the displacement owing to this force, referred to as the core field, is inversely proportional to the distance from the core, and the interference between the core fields induced by the multiple dislocations and their mirror images results in finite size corrections of various quantities. In the present work we directly observe the core force using the DFT calculation for configurations given by LES, and calculate the core field by the lattice Green’s function method [5] to estimate the finite size effect.

Fig. 7 shows the forces acting on each atom, F_i^c , calculated by DFT for the case of LES of the easy-core, hard-core, split-core and M position configurations in the 21×11 system. The core force for the smaller case of

15×9 is very close to the 21×11 case, and the maximum difference of forces between them is $0.02 \text{ eV } \text{\AA}^{-1}$. In the easy-core configuration, the distance between the innermost three atoms and the second innermost atoms is about 96% of that of a perfect crystal, and the second innermost atoms are pushed outward. In the hard-core configuration, the distance between the innermost three atoms is about 94% of that of a perfect crystal, and the innermost atoms are pushed outward more strongly than in the easy-core case.

The DFT energy of the LES, E_{LES}^{DFT} , also shows a very weak size dependence. Let us consider the relative value of E_{LES}^{DFT} with respect to the easy-core configuration divided by the number of dislocation, ΔE_{LES}^{DFT} . Hereafter the symbol Δ is also used for other quantities with the same meaning. This difference of energy mainly comes from the energy difference of core structure ΔE_c and the difference of the interaction energy between dislocations ΔE_{INT} . We assume that $\Delta E_{LES}^{DFT} = \Delta E_c + \Delta E_{INT}$ and E_{INT} is given by

$$\frac{\mu b^3}{2\pi} \left(-\log(r_{12}) + \sum_{i=1,2} \sum_j q_i q_j \log(r_{ij}) \right) \quad (6)$$

where $\mu = 57 \text{ GPa}$ is the shear modulus of the strain in $\{1\bar{1}0\}\langle 111 \rangle$ calculated by DFT, i and j denote the index of dislocation inside the cell and all the outside mirror images, respectively, $q_i = \pm 1$ is the helicity of the dislocation i and r_{ij} is the distance between dislocations i and j . Fig. 8 shows the dependence of ΔE_c of the hard-core, M

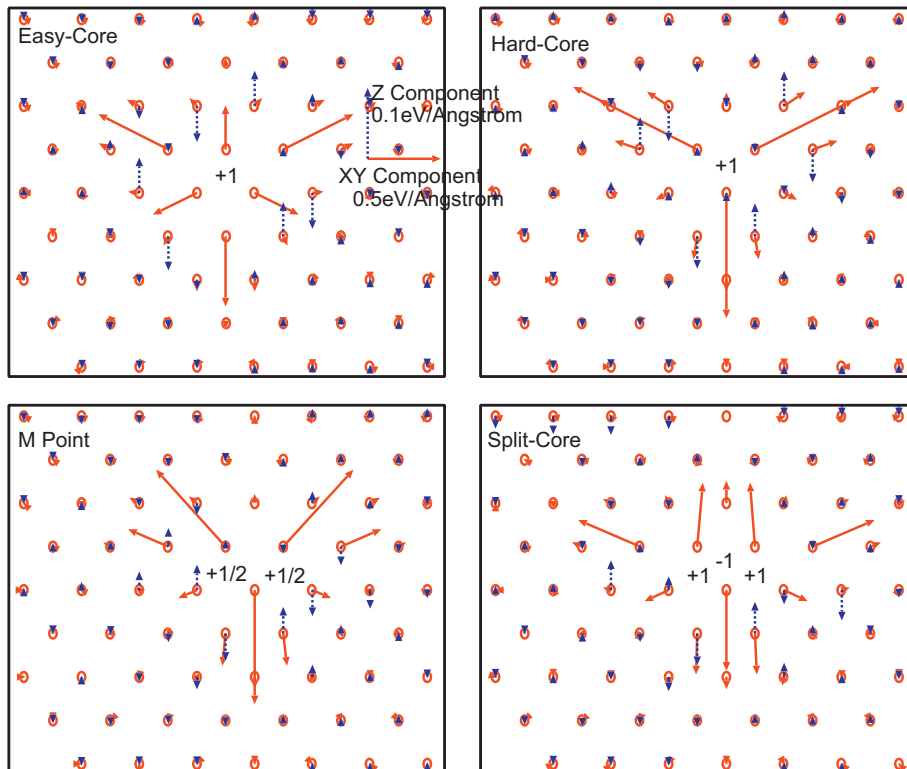


Fig. 7. Core forces of the easy-core, hard-core, split-core and M position configurations. Z-components of the force are shown by vertical arrows and exaggerated five times compared to the XY components.

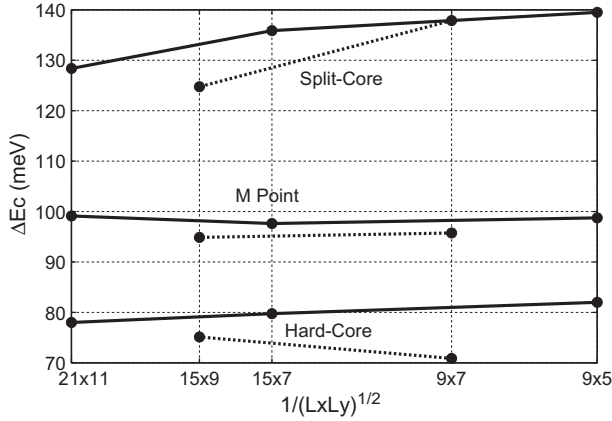


Fig. 8. The size dependence of the core energy ΔE_c of the hard-core, M point and the split-core configurations. Solid and dashed lines correspond to the data of the systems with the aspect ratio $\sqrt{3}L_y/L_x$ being greater and less than 1, respectively.

point and split-core configurations on the system size $L_x \times L_y$. Solid and dashed lines correspond to the data of the systems with the aspect ratio $\sqrt{3}L_y/L_x$ being greater and less than 1, respectively. These two cases show the opposite size dependence except for the split-core case in the 9×7 system size. From this result, the finite size effect for ΔE_c at the size 15×9 is estimated to be about 4 meV.

The DFT energy of the relaxed configuration is denoted by E_{RLX}^{DFT} and the energy difference $E_{RLX}^{DFT} - E_{LES}^{DFT}$ is denoted by E_{RLX}^{DFT} . This relaxation energy can be approximated by $-\frac{1}{2} \sum_i F_i^c u_i^c$, where u_i^c denotes the change in displacement by the relaxation. This change in displacement can be approximately calculated by the linear elasticity theory, and in the present work we use the lattice Green's function method. We assume that a small perturbation δ to a degree of freedom j induces a force $H_{ij}\delta$ on the degree of freedom i , and that the Hessian matrix H_{ij} , which is the inverse matrix of the lattice Green's function, is approximated well by that of a perfect crystal. Then the core field u_j^c can be obtained by solving the following linear equations:

$$\sum_j H_{ij} u_j^c = -F_i^c \quad (7)$$

To calculate H_{ij} , a perfect crystal system is prepared using the same system size and boundary condition as those for the dislocation calculation, and one atom is displaced by a small amount in each of the X , Y and Z directions. The forces induced on each atom is then observed using the DFT calculation with the same parameters as the dislocation calculations. We find that the induced forces are proportional to the amount of displacement up to 0.08 \AA , and that the force is only significant at the displaced atom and its nearest neighbors, while forces on the other atoms are negligible. If we denote by H_{ij}^{ab} the matrix element for the displacement of the atom i in the direction a and the displacement of the atom j in the direction b , the observed values are $H_{ii}^{XX} = H_{ii}^{YY} = -10.6 \text{ eV/\AA}^2$, $H_{ii}^{ZZ} = -6.03 \text{ eV/\AA}^2$ and $H_{ii}^{ab} = 0$ for all $a \neq b$ cases. For the

neighbor atom j located at the $+X$ direction of the atom i and displaced by $-b/3$ in the Z direction compared to the atom i , the matrix is $H_{ij}^{XX} = 3.32 \text{ eV/\AA}^2$, $H_{ij}^{YY} = 0.201 \text{ eV/\AA}^2$, $H_{ij}^{ZZ} = 1.00 \text{ eV/\AA}^2$, $H_{ij}^{XZ} = H_{ij}^{ZX} = 0.331 \text{ eV/\AA}^2$ and $H_{ij}^{XY} = H_{ij}^{YX} = H_{ij}^{YZ} = H_{ij}^{ZY} = 0$. Matrix elements for other neighbor atoms can be calculated from these values using the rotational symmetry.

The elastic constants expressed in the cubic axis derived from this matrix are $C_{11} = 237 \text{ GPa}$, $C_{12} = 104 \text{ GPa}$ and $C_{44} = 116 \text{ GPa}$, which are in reasonable agreement with the experimentally observed values $C_{11} = 243$, $C_{12} = 145$ and $C_{44} = 116 \text{ GPa}$. The calculated anisotropy ratio $2C_{44}/(C_{11} - C_{12}) = 1.74$ indicates that the elastic anisotropy is included in the matrix H_{ij} , although the ratio is smaller than the experimental value 2.36.

The relaxation energy can then be estimated from the lattice Green's function as follows:

$$E_{RLX}^{GF} = -\frac{1}{2} H_{ij}^{-1} F_i^c F_j^c \quad (8)$$

If E_{RLX}^{GF} agrees well with the actual value E_{RLX}^{DFT} , one can estimate the relaxation energy of an isolated dislocation, $E_{RLX}^{GF\infty}$, using the core force of only one dislocation and using a sufficiently large lattice in the calculation of u_i^c , and also estimate the finite size effect $E_{FSE}^{GF} = E_{RLX}^{GF\infty} - E_{RLX}^{GF}$. Finally, the Peierls energy ΔE_P for an isolated dislocation is estimated as $\Delta E_P = \Delta E^{DFT} - \Delta E_{INT} + \Delta E_{FSE}^{GF}$.

5. Results

Table 1 summarizes the energies of the various core positions shown in Fig. 6, calculated using the 15×9 system. For the calculation of E_{RLX}^{GF} , core forces smaller than 0.05 eV/\AA are omitted, and a periodic rectangle of 150×90 atoms system is used to calculate $E_{RLX}^{GF\infty}$. The agreement between E_{RLX}^{DFT} and E_{RLX}^{GF} is excellent, and we can use the Green's function method to estimate the finite size effect on the Peierls energy. Our estimate of the finite size effect is 2 meV for positions near the M point and the hard-core position, and 5 meV near the split-core position. Together with the 4 meV uncertainty of the finite size effect on ΔE_c , the numerical error for the Peierls potential is estimated to be 6 meV for P9, P16, P17 and P18, and 5 meV for the other cases. Fig. 9 shows a comparison of the core fields between the DFT calculations and the Green's function method for the case of easy-core, hard-core, M point and split-core configurations. The agreement is excellent, except near the core region. Considering that the finite size effect mainly comes from the long-range part of the core field, we expect that the error of the core field near the core region calculated by the lattice Green's function method does not affect the calculation of finite size effect E_{FSE}^{GF} .

The calculated values of the Peierls energy ΔE_P in Table 1 are fitted to a plane-wave expansion which accounts for the periodicity and symmetry as follows:

Table 1

DFT energies and calculated correction terms for various core positions for the system size 15×9 . All values are in meV. The numerical error for the Peierls energy ΔE_P is estimated to be 6 meV for P9, P16, P17 and P18, and 5 meV for the other cases. See the main text for details.

P	ΔE_{LES}^{DFT}	ΔE^{DFT}	E_{RLX}^{DFT}	E_{RLX}^{GF}	$E_{RLX}^{GF\infty}$	ΔE_{FSE}^{GF}	ΔE_{INT}	ΔE_P
P0	0	0	−215	−207	−227	0.0	0.0	0.0
P1	16	3	−240	−227	−247	−0.1	0.1	3.2
P2	19	11	−230	−218	−238	0.1	−0.2	11.5
P3	52	19	−280	−270	−289	0.2	0.2	19.2
P4	40	19	−258	−248	−270	−0.9	0.0	17.6
P5	56	41	−244	−240	−265	−2.0	−0.5	39.9
P6	83	31	−319	−311	−329	0.7	0.1	31.1
P7	69	30	−292	−284	−305	−0.4	0.1	29.9
P8	65	41	−264	−260	−285	−2.5	−0.2	38.7
P9	93	79	−242	−245	−274	−4.5	−0.8	75.2
P10	95	38	−329	−331	−348	1.6	0.0	39.3
P11	92	36	−326	−321	−339	1.2	0.1	37.0
P12	86	35	−316	−313	−333	−0.1	0.2	34.8
P13	79	36	−301	−296	−317	−0.3	0.1	35.3
P14	75	40	−285	−284	−308	−2.1	0.0	37.9
P15	74	51	−262	−265	−289	−2.3	−0.2	48.4
P16	81	64	−250	−255	−283	−3.5	−0.5	60.7
P17	97	81	−247	−252	−282	−4.9	−0.8	76.9
P18	124	113	−236	−251	−282	−5.5	−1.2	108.9

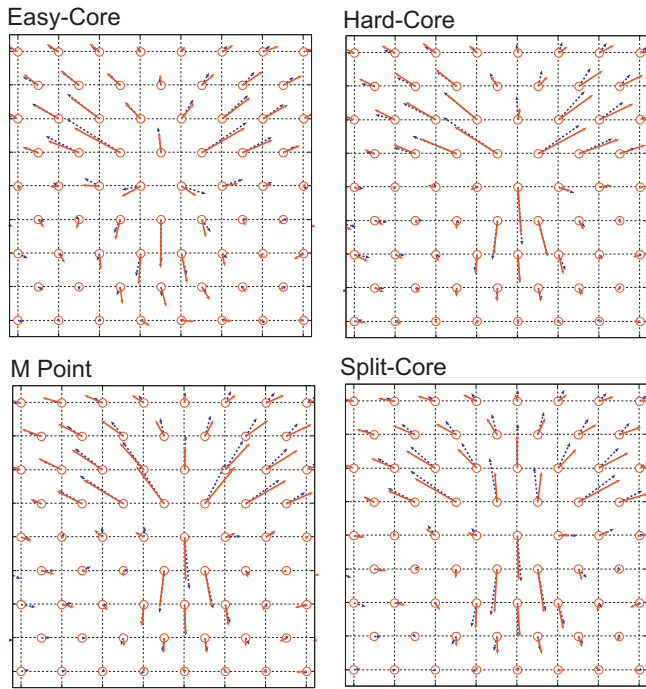


Fig. 9. A comparison of the core fields calculated by the DFT (solid red arrows) and the lattice Green's function method (dashed blue arrows), respectively. Only the XY components are shown for clarity, and they are exaggerated by a factor of 40. (For interpretation of the references to colour in this figure legend, the reader is referred to the web version of this article.)

$$\begin{aligned}
 E(\vec{r}) = & \sum_{\alpha} [C_1 f_e(x_{\alpha}) + C_2 f_o(x_{\alpha})] + \sum_{\alpha} [C_3 f_e(2x_{\alpha}) \\
 & + C_4 f_o(2x_{\alpha})] + C_5 [f_e(x_1 - x_2) + f_e(x_2 - x_3) \\
 & + f_e(x_3 - x_1)]
 \end{aligned} \quad (9)$$

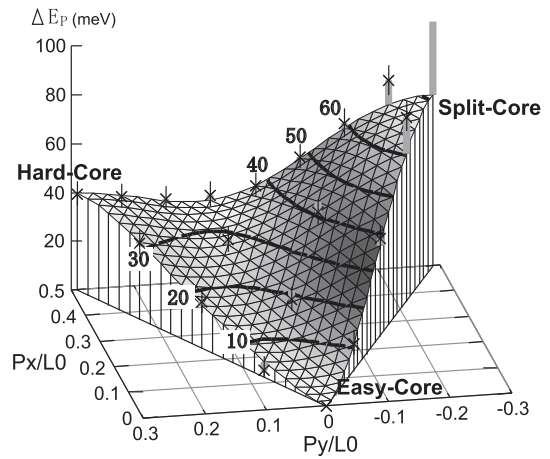


Fig. 10. Two-dimensional Peierls energy ΔE_P , obtained by DFT calculations. The curved surface is a plane-wave expansion fitted to the DFT results. The cross-symbols are the values of ΔE_P in Table 1; their relative values with respect to the fitted values are shown by gray perpendicular lines. The thin vertical lines are numerical errors of DFT calculations.

where $x_{\alpha} \equiv \vec{r} \cdot \vec{k}_{\alpha}$, k_{α} points toward three equivalent $\langle 1\bar{1}0 \rangle$ directions with a length $|k_{\alpha}| = \frac{4\pi}{\sqrt{3}L_0}$ and L_0 is the distance between adjacent easy-core positions, $f_e(x) = (1 - \cos(x))/2$ and $f_o(x) = \sin(x)/2$. The coefficients are $C_1 = 21.82$, $C_2 = -14.51$, $C_3 = 2.59$, $C_4 = -2.72$ and $C_5 = -2.89$ meV. Fig. 10 shows this fitted potential surface, with cross-symbols corresponding to the values of ΔE_P in Table 11 their relative values with respect to the fitted values are shown by perpendicular lines.

The Peierls energy profile on a line segment between the hard-core and the split-core positions is shown in Fig. 11, which is a dividing ridge between two basins of easy-core potential minima. The minimum in this plot gives a Peierls barrier for dislocation migration, and one can see that the

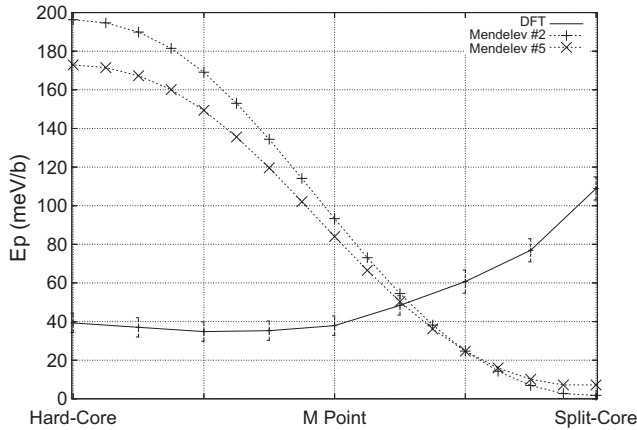


Fig. 11. Peierls energy profile of a line segment between the hard-core and split-core positions calculated by DFT. Dotted lines show calculation results obtained by two variants of the EAM potential in Ref. [13].

plot is nearly flat between the hard-core position and the M point. This indicates that the saddle point can be anywhere between these two points. However, energy minimization of a kink configuration will select the shortest path between the two easy-core positions, and the actual saddle point is expected to be near the M position. Fig. 11 also shows the energy profile calculated by two variants of the embedded atom method (EAM) potential by Mendelev et al. [13], which differ from the DFT results significantly. This difference results in widely different average slip directions, as will be demonstrated in later sections. The split-core position, which is metastable in the Mendelev potential, is actually unstable, as has been shown in Ref. [12].

Our final estimate for the Peierls barrier is 35 ± 5 meV per b , which is in good agreement with the experimental observations of 27–48 meV [2,14]. This result is also in good agreement with the DFT calculation using the SIESTA code, 28–33 meV [10].

Next, we investigate the effect of external stress on the Peierls energy. A uniform shear strain ϵ_{YZ} is applied to the system in the DFT calculations by increasing the Z component of the cell vector \mathbf{e}_2 by an amount $\epsilon_{YZ}e_2^Y$, where e_2^Y is the Y component of \mathbf{e}_2 . This strain exerts forces in the X direction on the two dislocations. We investigate four cases, for strain values of $\epsilon_{YZ} = 0\%$, 0.5%, 1.0% and 1.5%. When the two dislocations with opposite helicities move in the X direction by the same distance, change in the uniform strain component induced by this movement is canceled out and the uniform strain remains unchanged. We confirm that the variation in the uniform stress σ_{YZ} is at most 2% in the DFT calculation when the two dislocations move from the easy-core position to the M point.

The effect of the applied stress on the Peierls energy is given by the Peach–Koehler term as follows:

$$\{(\sigma * \vec{b}) \times \vec{l}\} \cdot \vec{r}, \quad (10)$$

where $\sigma * \vec{b}$ is a tensor–vector product of the stress and Burgers vector, \vec{l} is a vector parallel to the dislocation line

and its length is equal to the dislocation segment under consideration, and \vec{r} is a dislocation position. An additional effect of the applied stress, on the shape of the Peierls energy ΔE_P , has been reported in Ref. [15]. It is important to check the presence of this additional effect to model the behavior of dislocations under an applied stress.

When the Burgers vectors of the two dislocations are anti-parallel, the term in Eq. (10) cancels out and one cannot directly observe it. Instead, we observe separately the forces F_x and F_y acting on the two dislocations. By comparing the lattice stress $S_x = -F_x/b^2 \pm \sigma_{YZ}$ and $S_y = -F_y/b^2$ for the different strain cases, one can see whether the Peierls potential is affected by the applied stress or not.

Fig. 12 shows a schematic of the method of calculation for the lattice stress. Since the applied stress breaks the symmetry of inversion in the X direction, the lattice stress curve plotted against the reaction coordinate η can be asymmetric around $\eta = 1/2$, as shown by the solid line in Fig. 12. For the “plus” dislocation, its position between the easy-core and the adjacent M point which is on the $+X$ direction corresponds to the range $0 \leq \eta \leq 1/2$, while for the “minus” dislocation it corresponds to $1/2 \leq \eta \leq 1$. Observing the forces acting on the two dislocations separately, we can obtain the complete lattice stress curve.

Fig. 13 shows a comparison of the lattice stress for different applied shear strains. Observed values of the uniform stress σ_{YZ} which are subtracted from the force for each strain case are also shown by horizontal lines. Although the curves do not conform to a single line, the deviation of S_x is best described by shifting to the $-\eta$ direction as the strain is increased, while the shape of the curves of S_y changes slightly for strains greater than 1.0%. If the

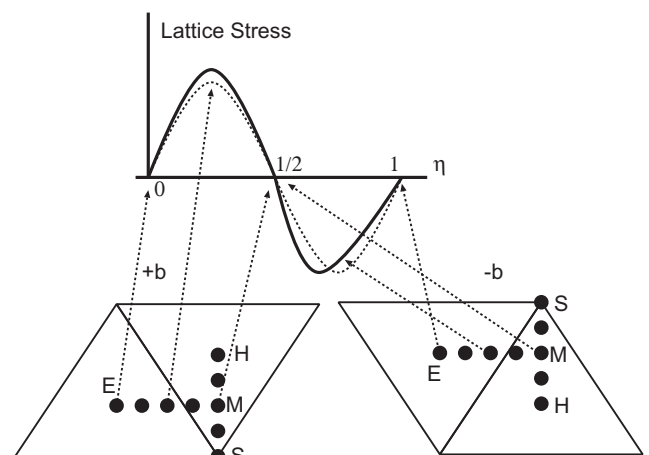


Fig. 12. Schematic of calculation of lattice stress curve from the forces acting on the two dislocations with opposite helicity. Black circles denote the dislocation positions where the lattice stress is observed in the DFT calculations. Solid and dotted curves represent the lattice stress of the zero stress and non-zero stress cases, respectively. Both dislocations are moved in the same direction, and the forces on dislocations with the positive and negative helicities are used to calculate the lattice stress for $0 \leq \eta \leq 1/2$ and $1/2 \leq \eta \leq 1$, respectively.

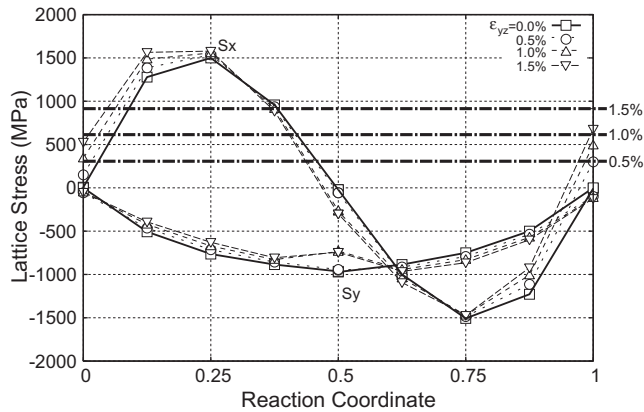


Fig. 13. Comparison of the lattice stress for different applied shear strains of $\epsilon_{yz} = 0\%$, 0.5% , 1.0% and 1.5% . The uniform stress σ_{yz} observed in the DFT simulation for each strain is shown by horizontal dashed lines.

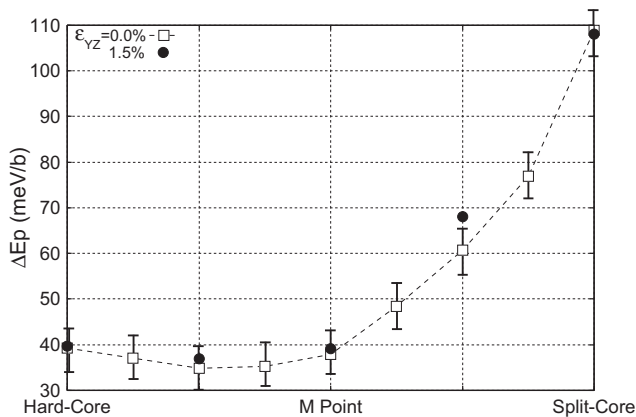


Fig. 14. Comparison of Peierls energy profile on a line segment between the hard-core and the split-core position for $\epsilon_{yz} = 0\%$ and 1.5% cases.

applied stress only shifts the curve and does not change its shape, the shape of ΔE_P remains unchanged. Fig. 14 shows a comparison of the Peierls energy profile of a line segment between the hard-core and split-core positions for the $\epsilon_{yz} = 0$ and 1.5% cases. The difference between the two cases is less than 5 meV in the saddle point region.

From these results, we conclude that the effect of the applied stress is described well by the linear elasticity theory given by Eq. (10) and its additional effect on the shape of E_P is very weak, at least up to 900 MPa, which is the maximum stress investigated in the present work. The Peierls stress, above which the Peierls energy landscape has no stable minima, is estimated from Eq. (9) to be 1000 ± 50 MPa. This stress is far stronger than the experimental estimation of ~ 400 MPa (such a discrepancy between atomistic models and experiment is a general tendency in bcc metals [16–19]). The Peierls stress is determined by the maximum slope of the potential energy, and one can estimate its lower bound by $\Delta E / \Delta x b^{-2}$, where ΔE is the saddle point energy and Δx is the distance between the easy-core position and the saddle point. Since the value of ΔE agrees well with

the experimental estimation and the lower bound Peierls stress calculated with $\Delta E = 30$ meV gives 690 MPa, which is still far stronger than the experimental estimation, this discrepancy of the Peierls stress cannot be attributed to the shape of the potential energy landscape but should be attributed to other phenomena, such as interactions between dislocations [16].

6. Line tension model

The dislocation mobility is determined by the formation enthalpy of a dislocation kink, a defect at which a dislocation line moves from one Peierls energy minimum to the next [17]. Fig. 15 depicts the kink nucleation mechanism of dislocation migration. As shown in the inset of the figure, the total dislocation enthalpy reaches a maximum when some part of the dislocation bulges and overcomes the Peierls barrier. After that, a fully formed kink pair moves in the opposite direction, lowering the total enthalpy as they separate until the whole dislocation line moves to the next minimum of the potential energy.

The kink formation enthalpy calculated from the molecular statics [20] or line-tension model adjusted on atomistic calculations [15,21] has been shown to reproduce the dislocation velocity in the molecular dynamics simulations. For a screw dislocation in bcc metals, the kink width is estimated as 10–20b [22], and a direct calculation of kink formation enthalpy requires at least several tens of slabs, which amount to thousands of atoms. Since plane-wave-based DFT of thousands of atoms is not feasible, we use the following line tension model to estimate the kink formation enthalpy:

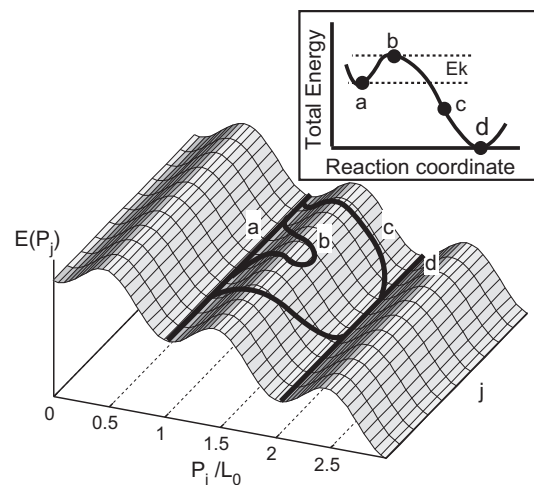


Fig. 15. Schematic of dislocation movement by the kink nucleation mechanism. (a) A straight dislocation lies in a valley of Peierls potential energy. (b) Some part of the dislocation bulges and overcomes the Peierls barrier. (c) A kink pair is fully formed and two kinks move in the opposite direction, lowering the total enthalpy as they separate. (d) Both kinks are absorbed at the boundary of the dislocation, completing the movement process.

$$E_{LT} = \frac{K}{2} \sum_j (\vec{P}_j - \vec{P}_{j+1})^2 + \sum_j \Delta E_P(\vec{P}_j) + \{(\sigma * b) \times \vec{l}\} \cdot \vec{P}_j \quad (11)$$

where K is a constant related to the elastic constants of the material, j is an index of thin slabs with the thickness b parallel to the Z axis, $\vec{P}_j = (P_j^x, P_j^y)$ is the position of a dislocation core in slab j , ΔE_P is the Peierls barrier per Burgers vector b obtained in the previous section, and the third term is the contribution from the external stress.

The constant K can be calculated by comparing the quadratic expansion of Eq. (11) in P_j^x and P_j^y with the expansion of $E_d(x^d + \delta)$ in δ , which is given as follows:

$$E_d(x^d + \delta) - E_d(x^d) \sim -\sum_i \delta_i F_i + \frac{1}{2} \sum_{ij} H_{ij} \delta_i \delta_j \quad (12)$$

The perturbation in x^d also changes $\bar{x}^o(x^d)$, but the change in x^o does not affect the energy. The matrix H_{ij} can be calculated from the change in the forces acting on each x^d as follows:

$$F_i(x^d + \delta) - F_i(x^d) = \sum_j H_{ij} \delta_j \quad (13)$$

First we demonstrate the calculation scheme of K using an EAM potential, and compare the kink shape predicted by the line tension model with the actual kink shape obtained in MD simulation. An isolated screw dislocation of length $60b$ is provided using the system consisting of 1452 atoms per layer. With a Mendelev potential of the variant 5 [13], this system is fully relaxed to the easy-core configuration while the outermost atoms are fixed to the linear elasticity solutions. Then one atom in the innermost three atom columns is displaced in the $+Z$ direction by 0.01 \AA , and a force acting on every atom is calculated using the EAM potential. The induced force on the two atoms which are located directly above and below the displaced atom is found to be 29 meV \AA^{-1} in the Z direction, while that on the displaced atom itself is -82 meV \AA^{-1} in the same direction. Forces induced on the other atoms are negligible. Thus H_{ij} is calculated to be $H_{ii} = 8.2 \text{ eV \AA}^{-2}$ for the diagonal element and $H_{ij} = -2.9 \text{ eV \AA}^{-2}$ for the neighboring pair on the same atomic row. If we denote the Z displacement of the innermost three atoms on the layer j by $z_{j,1}$, $z_{j,2}$ and $z_{j,3}$, the total energy can be expanded in these quantities as

$$\frac{1}{2} \sum_j \sum_{a=1,2,3} A z_{j,a}^2 + K_0 (z_{j,a} - z_{j-1,a})^2 \quad (14)$$

with $A = 2.4 \text{ eV \AA}^{-1}$ and $K_0 = 2.9 \text{ eV \AA}^{-1}$. Together with Eqs. (3) and (11), we get $K = \frac{9}{32} K_0 = 0.816 \text{ eV \AA}^{-2}$ for the Mendelev potential. The Peierls energy landscape of the same potential is calculated using a single-layer, isolated dislocation configuration, and fitted to the form of Eq. (9). The coefficients are $C_1 = 40.4$, $C_2 = 66.9$, $C_3 = -0.1$, $C_4 = 2.3$ and $C_5 = 0.6 \text{ meV}$.

Fig. 16 shows a comparison of kink shapes of the MD simulation and the line tension model with these parameters. In addition to the good agreement in the kink shape

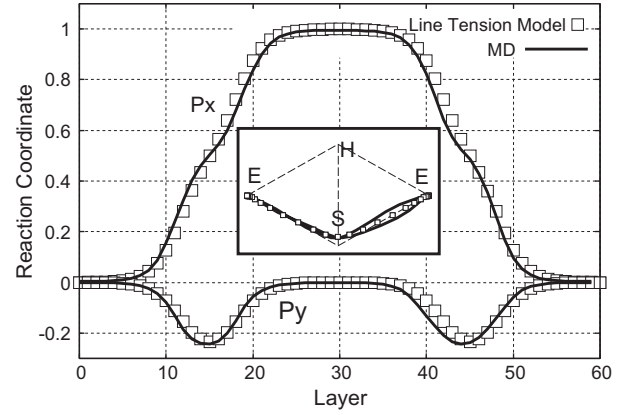


Fig. 16. Comparison of the kink shapes of the MD simulation and the line tension model. P_x and P_y are normalized by the distance between two easy-core positions. The inset shows the two-dimensional kink shape in the XY plane for both cases.

in the x direction, which was shown in previous studies using the line tension model [15], the kink shape in the y direction also shows excellent agreement. The kink pair energy calculated by the MD relaxation is 0.78 eV , while the line tension model gives 0.69 eV . It has been shown that the kink shape and energy is asymmetric between the two types of kinks in the MD calculations [22]. This means that there should be higher-order terms of the gradient $\vec{P}_j - \vec{P}_{j-1}$ in the energy, and the difference of the energy between the MD and the line tension model can be attributed to this term. As a whole, these results clearly demonstrate the validity of the calculation scheme of K presented above. By a simple scaling argument, one can show that the kink formation energy is proportional to $\sqrt{KE_P}$, and fortunately the uncertainty in K only modestly affects the estimate of kink formation energy.

To estimate the value K in the DFT calculation, a single-layer hexagonal system consisting of 108 atoms, which contains a single easy-core configuration in the center, is prepared and relaxed, while the outermost 33 atoms are fixed. The obtained configuration planes are then stacked on each other to form a three-layer system, and one of the innermost atoms is displaced in the Z direction by 0.01 \AA . The forces induced by this displacement are calculated using the DFT. From the MD result and the DFT calculation of the perfect crystal, we found that forces on the second or farther neighboring atoms can be ignored, and that a three-layer system is suffice to calculate the matrix H_{ij} . The force induced on the two atoms located directly above and below the displaced atom is found to be $0.0308 \text{ eV \AA}^{-1}$; the forces on the atoms in the other atomic column are negligible. From this result, we get $K_0 = 3.08 \text{ eV \AA}^{-2}$, and consequently $K = 0.866 \text{ eV \AA}^{-2}$.

The kink pair nucleation enthalpy E_k and its dependence on the applied stress is calculated by applying the transition state search method [23] to the model (11). Fig. 17 shows the kink shape predicted from the line tension model, when there is no applied stress. The kink pair energy and the kink

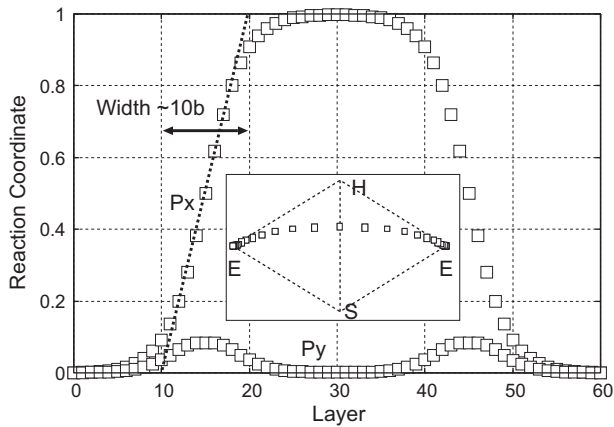


Fig. 17. Kink shape obtained from the line tension model with the parameters given by the DFT calculations. P_x and P_y are normalized by the distance between two easy-core positions. The kink width is estimated to be $10b$. The inset shows the two-dimensional kink shape in the XY plane.

width are estimated to be 0.73 eV and $10b$, respectively, which are in good agreement with previous studies [22] and an experimental estimate [24]. Since the kink width is proportional to $b\sqrt{K/E_p}$ and E_p is much higher than that of the Mendelev potential, the kink width is much shorter compared to the Mendelev potential case.

Fig. 18 shows the dependence of E_k on the applied stress for three maximum resolved shear stress directions, $[111](1\bar{1}0)$, $[111](11\bar{2})$ (twinning) and $[111](2\bar{1}\bar{1})$ (anti-twinning), together with experimentally observed values from Ref. [24] and their linear fit. For the case of stress in the $(1\bar{1}0)$ plane, the direction of a dislocation migration coincides with the stress direction, while for the case of twinning and anti-twinning, the high Peierls barrier around the split-core position prohibits a direct migration in the $\{211\}$ planes and the macroscopic slip in the $\{211\}$ planes is realized by random successive migrations in the two equivalent $\{110\}$ planes, assuming that the screw dislocation is terminated by

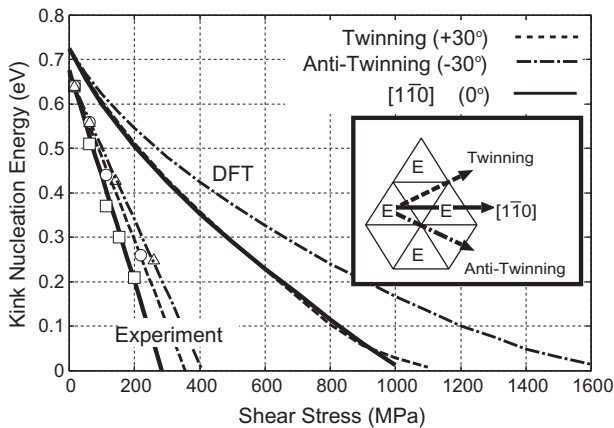


Fig. 18. Stress dependence of the kink nucleation enthalpy for three stress directions, $[111](1\bar{1}0)$, $[111](11\bar{2})$ (twinning) and $[111](2\bar{1}\bar{1})$ (anti-twinning). Experimental data from Ref. [24] are also shown as symbols, together with straight line fits.

either a free surface or a periodic boundary. A trace of this random migration has been experimentally observed as a wavy pattern on a free surface of a thin film [2]. When the screw dislocation is part of a loop, the edge part energetically favors a straight line and random migration is expected to be suppressed. The overall tendencies shown in Fig. 18, such as the non-Schmit behavior that a slip in the twinning direction is easier than in the anti-twinning direction, agrees with the experiment in Ref. [24], except for the already discussed discrepancy of the Peierls stress.

The average slip direction at a finite temperature is calculated using the Brownian dynamics simulation:

$$\vec{P}_j(t + \Delta t) = \vec{P}_j - \Delta t \nabla_j E_{LT} + \sqrt{2k_B T \Delta t} \vec{\eta}_j \quad (15)$$

where ∇_j denotes a derivative with respect to \vec{P}_j , T is the temperature, k_B is the Boltzmann constant and $\vec{\eta}_j$ is a two-component Gaussian random variable whose average and variance are 0 and 1, respectively. It should be noted that the time scale in Eq. (15) does not correspond to the physical one, and any momentum effect is not incorporated. However, Eq. (15) is able to capture the entropic effect on the migration frequency and the interaction between kinks. A time step of $\Delta t = 1.1 \times 10^{-3}$ is used, which ensures that the change in \vec{P}_j at each step is at most 3% of the distance between two easy-core positions, and the iteration is repeated 10^5 times for each case.

Fig. 19 shows the dependence of the average slip direction on the stress and temperature, for the case of shear stress in the $[111](1\bar{1}0)$ direction. The angle is relative to the $(1\bar{1}0)$ plane and is defined as positive for the twinning direction. Similar plots have been obtained based on the MD simulations [9,25], and the main difference between the present result and the MD simulations is the magnitude of the deviation from the $(1\bar{1}0)$ plane. For all the cases studied here, it is less than 2° , in contrast to the MD results, in which the

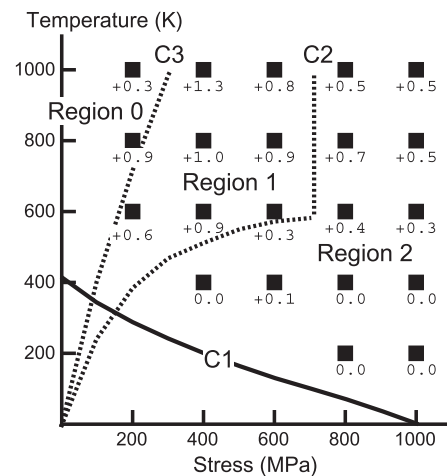


Fig. 19. Temperature and stress dependence of the average slip direction, relative to the maximum resolved shear stress direction of $[111](01\bar{1})$. The curves C1, C2 and C3 are the boundaries between different slip behavior regions, calculated from the difference between kink nucleation energies in different directions. See the main text for details.

deviation is as large as 20° . Experimental observation of dislocation motion [2] indicates that the slip plane for the case of maximum resolved shear stress in the $\langle 111 \rangle (1\bar{1}0)$ direction is primarily $(1\bar{1}0)$, and we conclude that the deviation of the slip direction in MD is an artifact of the EAM empirical potential. The three lines C1, C2 and C3 in Fig. 19, which separate the regions of different slip behavior, are given by the equations $T = E_k^0/20k_B$, $T = (E_k^+ - E_k^0)/2k_B$ and $T = (E_k^- - E_k^0)/2k_B$, respectively, where E_k^0 , E_k^+ and E_k^- denote the kink nucleation enthalpy to the neighbor easy-core configuration located in the directions of 0° , $+60^\circ$ and -60° , respectively, for a given value of applied shear stress in the $[111](1\bar{1}0)$ direction calculated using the line tension model. Below C1, the kink nucleation is so rare that we cannot obtain sufficient data. Above C2, nucleation in the $+60^\circ$ direction becomes comparable to that in the 0° direction and the average slip direction becomes positive. When the applied stress is greater than 800 MPa, the kink nucleation in this direction becomes unstable and eventually becomes a kink pair in the 0° direction, and the curve C2 becomes a vertical line at 800 MPa. Above C3, kink nucleation in the 0° , $+60^\circ$ and -60° directions all becomes comparable and the average slip direction decreases as the temperature is increased.

Fig. 20 shows how the applied stress affects the nucleation energies E_k^0 , E_k^+ and E_k^- . In the present study, the migration paths are close to a straight line and the contribution of the applied stress σ to the Peierls barrier is

approximately proportional to $\sigma \cos(\theta)\chi$, where $0 \leq \chi \leq 1$ denotes a reaction coordinate of the dislocation migration and $\theta = 0, +60^\circ$ and -60° . The migration path for the $+60^\circ$ case can bend toward the energetically favorable direction and the migration energy is further lowered, while for the -60° case the high energy of the split-core position prevents the path from bending to the energetically favorable direction and the migration energy is slightly higher than the $+60^\circ$ case. Thus we have $E_k^0 < E_k^+ < E_k^-$, in which case the stress and temperature dependence of the slip direction in Fig. 19 is reproduced.

For the case of the empirical EAM potential, the migration path passes through the split-core positions and the effect of the applied stress differs significantly from the present study case, as shown in Fig. 20(b). The migration energies for the 0° and -60° cases are almost the same, since the saddle point of the migration for these two cases are close together even though the corresponding atomic configurations differ. Consequently, the average slip direction becomes close to -30° as soon as the temperature is high enough to overcome the small energy difference between the 0° and -60° migrations. The double-humped potential shape also causes discontinuity in the kink nucleation enthalpy at a certain applied stress [26].

7. Summary and conclusion

Essential properties of a screw dislocation in bcc iron have been calculated and determined by plane-wave-based DFT calculations. The properties of dislocation kinks are determined using a line tension model which is based on the DFT results. Our findings are summarized as follows: (i) a screw dislocation migrates from one easy core position to an adjacent easy core position, following a nearly straight path; (ii) the saddle point of the migration is around a midpoint of two easy-core positions, at which the Peierls barrier is estimated to be 30–40 meV; (iii) a kink pair nucleation enthalpy is estimated to be 0.73 eV when no external stress is applied; (iv) when the maximum resolved shear stress is in the $\langle 111 \rangle \{1\bar{1}0\}$ direction, the average slip direction remains in the $\{1\bar{1}0\}$ plane with a deviation of less than 2° ; (v) when the maximum resolved shear stress is in the $\langle 111 \rangle \{2\bar{1}1\}$ direction, two equivalent $\{1\bar{1}0\}$ slips are activated randomly; and (vi) the Peierls stress is estimated to be 1000 MPa, with a lower bound of 620 MPa.

These results are consistent with experimental estimation, except for the far larger value of the Peierls stress (vi) compared to the experimental estimate. This discrepancy in the Peierls stress between atomic scale calculations and experiments is a general tendency in bcc metals, and we foresee that some mesoscopic modeling is required, such as the pile-up model proposed by Gröger et al. [16], to relate the calculated Peierls stress to the experimentally estimated yield stress in the zero temperature limit. Points (iv) and (v) are in clear contrast to the molecular dynamics simulations of bcc iron [9]. This is because the fundamental properties of migration for a screw dislocation have not been included

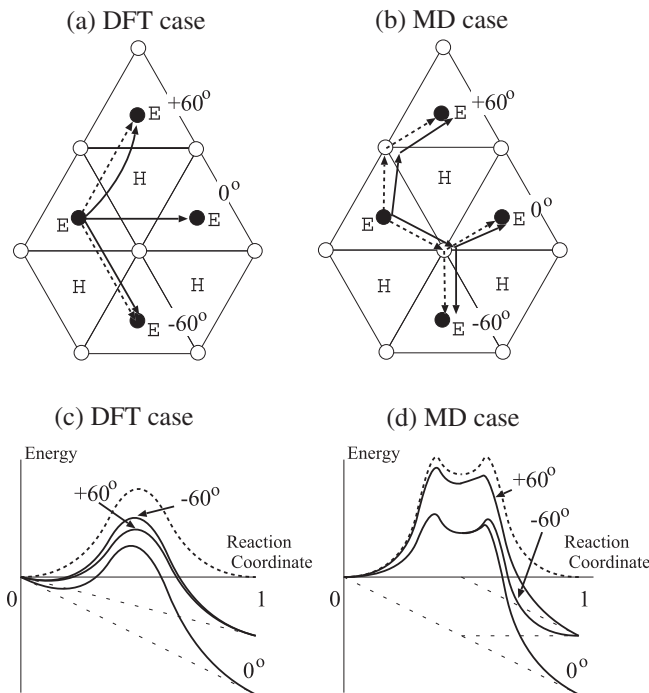


Fig. 20. Schematic of the effect of the applied stress on the average slip direction for the cases of (a) the present study and (b) the empirical EAM potential. Solid and dotted lines show migration pathways with and without the applied stress, respectively. (c and d) Schematic behavior of the Peierls barrier for both cases. See the main text for details.

in the fitting targets in the previous development of empirical potentials in bcc metals. Recently, an improved EAM potential has been developed by Gordon et al. [27] in an effort to reproduce both the symmetric easy-core structure and the single-humped Peierls energy. Gordon et al. concluded that conventional EAM potential is not capable of reproducing these two properties simultaneously. Further improvements in EAM potential based on the dislocation migration properties obtained in the present work, possibly by including the anisotropic terms or the magnetic degrees of freedom [28] in the potential, are strongly expected for the reliable simulation of plastic deformation in bcc iron.

Acknowledgements

We thank F. Willaime, L. Proville, L. Ventelon, E. Clouet and J. Marian for helpful discussions.

Appendix A. Anisotropic elasticity

Owing to the elastic anisotropy, the elastic constants in the Cartesian coordinates in Fig. 3 change from the cubic axis case by the amounts

$$\begin{aligned}\Delta C_{xx,xx} &= \Delta C_{yy,yy} = -A/2, \quad \Delta C_{zz,zz} = -2A/3, \quad \Delta C_{yy,zz} \\ &= \Delta C_{zz,xx} = A/3, \quad \Delta C_{xx,yy} = A/6, \quad \Delta C_{zx,zx} = \Delta C_{yz,yz} \\ &= A/3, \quad \Delta C_{xy,xy} = A/6, \quad \Delta C_{xx,zx} = \Delta C_{xy,yz} = -\frac{A}{3\sqrt{2}}\end{aligned}$$

and $\Delta C_{yy,zx} = \frac{A}{3\sqrt{2}}$, where $A = C_{11} - C_{12} - 2C_{44}$ is the anisotropy parameter. The isotropic linear elasticity solution for the $\langle 111 \rangle$ screw dislocation has components ϵ_{yz} and ϵ_{xz} , and induces excess stress fields $\sigma_{xx} = -A'\epsilon_{yz}$, $\sigma_{yy} = A'\epsilon_{zx}$ and $\sigma_{xy} = -A'\epsilon_{yz}$, where $A' = \frac{A}{3\sqrt{2}}$. However, these excess stress fields satisfy the equilibrium condition

$\sum_b \partial_b \sigma_{ab} = 0$ and the solution itself is identical to the isotropic case.

References

- [1] Kim JY, Jang D, Greer JR. Acta Mater 2010;58:2355.
- [2] Caillard D. Acta Mater 2010;58:3493; Caillard D. Acta Mater 2010;3504.
- [3] Spitzig WA. Acta Metal 1970;18:1275.
- [4] Vitek FV. Prog Mater Sci 2011;56:557.
- [5] Woodward C, Rao SI. Phys Rev Lett 2002;88:216402.
- [6] Frederiksen S, Jacobsen K. Philos Mag 2003;83:365.
- [7] Clouet E, Ventelon L, Willaime F. Phys Rev Lett 2009;102:055502.
- [8] Ventelon L, Willaime F. Philos Mag 2010;90:1063.
- [9] Chaussidon J, Fivel M, Rodney D. Acta Mater 2006;54:3407.
- [10] Ventelon L, Willaime F. J Comput-Aid Mater Des 2007;14:85.
- [11] Clouet E. Phys Rev B 2011;84:224111; Clouet E, Ventelon L, Willaime F. Phys Rev B 2011;84:224107.
- [12] Ventelon L. These de l'Universite Claude Bernard Lyon 2008;1.
- [13] Mendelev MI, Han S, Srolovitz DJ, Ackland GJ, Sun DY, Asta M. Phil Mag A 2003;83:3977.
- [14] Douin J, Castany P, Pettinari-Sturmelt F, Coujou A. Acta Mater 2009;57:466.
- [15] Rodney D, Proville L. Phys Rev B 2009;79:094108.
- [16] Gröger R, Vitek V. Philos Mag Lett 2007;87:113.
- [17] Domain C, Monnet G. Phys Rev Lett 2005;95:215506.
- [18] Segall DE, Strachan A, Goddard III WA, Ismail-Beigi S, Arias T. Phys Rev B 2003;68:014104.
- [19] Gröger R, Bailey AG, Vitek V. Acta Mater 2008;56:5401.
- [20] Rodney D. Phys Rev B 2007;76:144108.
- [21] Edagawa K, Suzuki T, Takeuchi S. Phys Rev B 1997;55:6180.
- [22] Ventelon L, Willaime F, Leyronnas P. J Nucl Mater 2009;286–388:26.
- [23] E W, Ren W, Vanden-Eijnden E. Phys Rev B 2002;66:052301.
- [24] Spitzig WA, Keh AS. Acta Metal 1970;18:1021.
- [25] Marian J, Cai W, Bulatov V. Nat Mater 2004;3:158.
- [26] Gordon PA, Neeraj T, Li Y, Li J. Model Simul Mater Sci Eng 2010;18:085008.
- [27] Gordon PA, Neeraj T, Mendelev MI. Philos Mag 2011;91:3931.
- [28] Lavrentiev M Yu, Dudarev SL, Nguyen-Manh D. J Appl Phys 2011;109:07E123.